

Article

Facile Synthesis of Flower-Like TiO₂-Based Composite for Adsorption–Photocatalytic Degradation of High-Chroma Methylene Blue

Mengqi Tian ^{1,2,3}, Jingjing Wang ⁴, Runjun Sun ^{3,*}, Mu Yao ³ and Lianbi Li ² 

¹ National Engineering Laboratory for Modern Silk, College of Textile and Clothing Engineering, Soochow University, Suzhou 215123, China; mengqitian0403@xpu.edu.cn

² School of Science, Xi'an Polytechnic University, Xi'an 710048, China; xpu_lilianbi@163.com

³ School of Textile Science and Engineering, Xi'an Polytechnic University, Xi'an 710048, China; yaomu1930@163.com

⁴ Suzhou Kaikai Technology Project Consulting Service Co., Ltd., Suzhou 215021, China; jingjing_wangsz@163.com

* Correspondence: sunrunjun@xpu.edu.cn

Abstract: A flower-like TiO₂-based composite (denoted as Zn-Ti-6) was prepared using a flower-like zinc oxide template for adsorption–photocatalytic degradation of high-chroma methylene blue. The reaction took place in an alkaline environment following hydrochloric acid treatment to remove the template and form TiO₂-based composite. Sodium hydroxide played both roles of morphology-directing agent and reactive etchant. The possible mechanism for the formation of flower-like Zn-Ti-6 was proposed. The adsorption and photocatalytic degradation behavior of Zn-Ti-6 on methylene blue (MB) removal was also investigated. The results revealed that Zn-Ti-6 showed better adsorption and photocatalytic degradation performance than TiO₂ nanoparticles owing to its much larger specific surface area, more abundant hydroxyls, and lower photoluminescence intensity. The adsorption and photocatalytic degradation data of Zn-Ti-6 were well fitted to the pseudo-second-order and pseudo-first-order kinetics models, respectively. The excellent adsorption performance of Zn-Ti-6 is largely beneficial to the subsequent photocatalytic degradation performance for high-chroma wastewater treatment. Overall, this study contributes a facile fabrication strategy for flower-like TiO₂-based composite to achieve the adsorption–photocatalytic degradation of high-chroma wastewater.

Keywords: flower-like TiO₂-based composite; alkaline hydrothermal; zinc oxide template; adsorption–photocatalytic degradation; high-chroma wastewater treatment



Citation: Tian, M.; Wang, J.; Sun, R.; Yao, M.; Li, L. Facile Synthesis of Flower-Like TiO₂-Based Composite for Adsorption–Photocatalytic Degradation of High-Chroma Methylene Blue. *Catalysts* **2021**, *11*, 515. <https://doi.org/10.3390/catal11040515>

Academic Editors: Kelvin H.-C. Chen and Jong-Chin Huang

Received: 31 March 2021

Accepted: 15 April 2021

Published: 20 April 2021

Publisher's Note: MDPI stays neutral with regard to jurisdictional claims in published maps and institutional affiliations.



Copyright: © 2021 by the authors. Licensee MDPI, Basel, Switzerland. This article is an open access article distributed under the terms and conditions of the Creative Commons Attribution (CC BY) license (<https://creativecommons.org/licenses/by/4.0/>).

1. Introduction

With the rapid development of the textile industry, the resultant organic water pollutions pose a long-term threat to the environment and human health [1,2]. The wastewater from textile dyeing containing high concentrations of dyestuffs, such as methylene blue (MB), is one of the most harmful industrial effluents [3,4]. Currently, a large number of photocatalytic degradation technologies have been developed to remove the dye residues from wastewater. However, the photocatalytic degradation technology performs poorly, especially for high-chroma wastewater. The reason is that the poor light transmittance of high-chroma wastewater suppresses the photocatalyst performances [5–7]. In addition, adsorption technology has been widely applied in the field of wastewater treatment for its simple operation and generality [8]. For example, activated carbon is one of the most common adsorbents. However, adsorption alone cannot degrade toxic substances or dyes into non-toxic and pollution-free H₂O and CO₂, etc. [9,10]. Recently, an adsorption–photocatalytic degradation strategy has been proposed by many researchers [11–13].

To date, there are two main strategies to achieve adsorption and photocatalytic degradation. A typical method is to stabilize the photocatalyst (titanium dioxide (TiO₂), zinc

oxide (ZnO), etc.) on the surface of the adsorbent (zeolites, clays, activated carbon, etc.) [14–16]. However, the uneven distribution of the photocatalyst exerts a great impact on the photocatalytic degradation efficiency. An alternative method is to improve the adsorption capacity of the photocatalyst itself through structural adjustment [17,18]. For example, TiO₂ is cost-effective, stable, and capable of degrading most pollutants [19]. Kasuga et al. synthesized a new TiO₂ nanotube through a simple wet chemical method with a 5–10 M sodium hydroxide (NaOH) solution [20]. The TiO₂ nanotube, featuring a large specific surface area, displayed not only excellent adsorbing behaviors, but also a certain photocatalytic activity. Since then, a series of relevant work on such material was implemented to further enhance its properties [21–23].

The performance of titanate can be improved by engineering the micro/nanoarchitecture morphology, such as three-dimensional (3D) hierarchical architectures [24]. The 3D hierarchical architectures can avoid the aggregation of low-dimensional nanomaterials, increase the reaction contact surface of the materials, and facilitate the adsorption and photocatalytic performances of the materials. Kuang et al. reported a facile synthesis of protonated flower-like titanate through one-step solvothermal method in the presence of hexamethylenetetramine [25]. The flower-like titanate possessed an extremely large surface area and displayed excellent adsorption performance. The formation of the flower-like titanate is attributed to the intercalation of amino-derivatives or NH₄⁺ of hexamethylenetetramine. Wang et al. investigated a facile strategy to prepare hollow 3D hierarchical titanate microspheres through the NaOH hydrothermal process. The manipulation of titanate morphology by changing the NaOH concentrations led to the evolution of different morphologies based on approach [26]. Zhang et al. synthesized a 3D hierarchical hollow sodium titanate microsphere via a silica microsphere template-assisted method. The silica microspheres were finally removed by the NaOH hydrothermal process [27]. The samples obtained were with a high surface area and the typical MB adsorption capacity. Although there are many studies that demonstrate the enhanced adsorption and photocatalytic capacities of 3D hierarchical titanate, few reports as yet reflect the synthesis of 3D hierarchical TiO₂-based composite [28,29]. Significantly, it is still a great challenge to synthesize 3D hierarchical TiO₂-based composite and study their formation mechanisms and performances.

Herein, we developed a facile alkaline hydrothermal procedure to prepare flower-like TiO₂-based composite for adsorption–photocatalytic degradation, and the proposed synthesis mechanism is shown in Figure 1. NaOH was a morphology-directing agent and reactive etchant. The flower-like ZnO was synthesized and used as a sacrificial template. The proper NaOH concentration contributed to form a flower-like ZnO template and further formed the sodium titanate, which was produced by the reaction of TiO₂ and NaOH. Sodium titanate self-assembled onto the ZnO template to form flower-like morphology. After hydrochloric acid (HCl) treatment, the ZnO template was completely removed, and sodium titanate was converted into TiO₂-based composite. Furthermore, the formation mechanism of TiO₂-based composite with different morphologies obtained under different NaOH concentrations was studied and proposed. Moreover, the adsorption and photocatalytic performances of the flower-like TiO₂-based composite obtained toward MB solution were investigated and compared with those of TiO₂ nanoparticles.

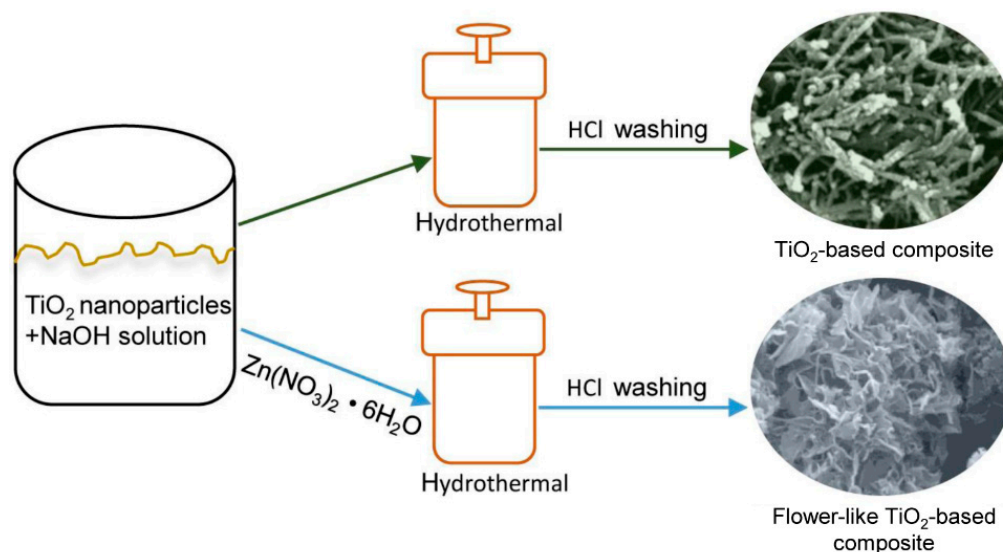


Figure 1. The proposed synthesis mechanism for flower-like TiO_2 -based composite.

2. Results and Discussion

2.1. Characterization

2.1.1. Morphologies

To understand the formation mechanism of the flower-like TiO_2 -based composite, the morphology depending on NaOH concentration was investigated from field emission scanning electron microscopy (FESEM) and transmission electron microscopy (TEM), as shown in Figure 2. The prepared samples were denoted as Zn-Ti-X, and samples without P25 or $\text{Zn}(\text{NO}_3)_2 \cdot 6\text{H}_2\text{O}$ were also prepared following the same process, named Zn-X or Ti-X for comparison, where X = 4, 5, 6, 7, and 8 M represented NaOH concentration in the precursor solution. From Figure 2a, it can be seen that TiO_2 nanoparticles (P25) were spherical particles. In addition, the TEM of P25 presented a granular structure with a diameter of about 20–30 nm in Figure 2b. In Figure 2c,d, flower-like structures were formed by a hydrothermal route in the presence of zinc nitrate hexahydrate ($\text{Zn}(\text{NO}_3)_2 \cdot 6\text{H}_2\text{O}$) and NaOH, and the petals were typical prismatic shape with a pencil-like end top. The flower-like structure and petals were destroyed in Figure 2d, compared with the intact flower and petals in Figure 2c. This suggests that the flower-like structure was dissolved and destroyed when the concentration of NaOH solution was 5 M. In addition, the color of the sample was white in Figure 2c, while the sample was light yellow in Figure 2d. As shown in Figure 2e, Ti-5 exhibited a tubular or rod-like structure when the precursors were P25 and NaOH (5 M). The morphologies of the samples prepared by $\text{Zn}(\text{NO}_3)_2 \cdot 6\text{H}_2\text{O}$, P25, and different concentrations of NaOH solutions were shown in Figure 2f,j, respectively. It can be clearly seen that the morphologies of the samples changed greatly with NaOH concentration. When NaOH concentration was 5 M, the flower-like structure with flake petals was as shown in Figure 2f. The diameter of the flower-like structure was around 3 μm . When NaOH concentration was increased to 6 M (Figure 2g), the sample was still presented as a flower-like structure. However, the petals were significantly thinner than 5 M. The TEM image in Figure 2h also shows that 6 M NaOH concentration induced the formation of very thin petals. Comparing Figure 2b,h, it can be clearly seen that P25 changed from granular to very thin flakes, and the edges of some flakes had obviously curled. A possible explanation for this phenomenon is that the Ti–O bond of P25 particles was broken and stripped into small nanosheets by concentrated NaOH during the process of hydrothermal reaction. Then, these small nanosheets were interconnected to form a large nanosheet structure due to the oxidation of hydroxyls at the original nanosheet edges [30]. With an increase in NaOH concentration (7 M and 8 M), the sample separately presented thinner flakes and tubular (or rod-like) structure (Figure 2i,j).

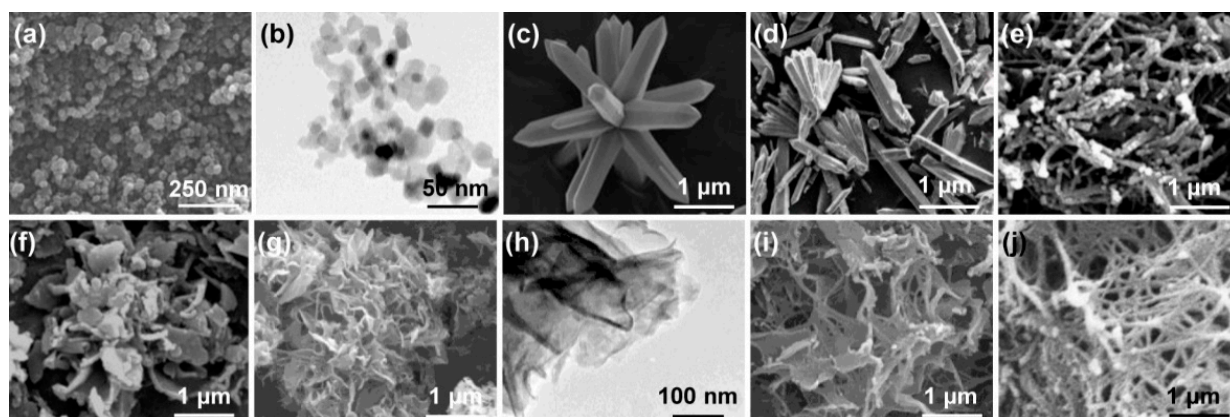


Figure 2. FESEM images of (a) P25, (c) Zn-4, (d) Zn-5, (e) Ti-5, (f) Zn-Ti-5, (g) Zn-Ti-6, (i) Zn-Ti-7, and (j) Zn-Ti-8; TEM images of (b) P25, and (h) Zn-Ti-6.

The possible mechanisms for these phenomena were considered to be as follows.

On the one hand, $\text{Zn}(\text{NO}_3)_2 \cdot 6\text{H}_2\text{O}$ reacted to produce flower-like ZnO at an appropriate NaOH concentration [31,32]. However, as the concentration of NaOH increased, the resulting flower-like ZnO was dissolved and destroyed [33]. On the other hand, P25 could form white precipitated sodium titanate under the condition of concentrated NaOH and form a TiO_2 -based composite after washing with HCl [34]. When $\text{Zn}(\text{NO}_3)_2 \cdot 6\text{H}_2\text{O}$, P25, and NaOH were present at the same time, the possible formation mechanism is described as follows: first, $\text{Zn}(\text{NO}_3)_2 \cdot 6\text{H}_2\text{O}$ and NaOH formed flower-like ZnO; second, the P25 particles were peeled off and adhered to form flower-like sodium titanate on the ZnO template [35]. In other words, both $\text{Zn}(\text{NO}_3)_2 \cdot 6\text{H}_2\text{O}$ and P25 were consuming NaOH. When the concentration of NaOH was appropriate, flower-like sodium titanate was formed on the flower-like ZnO template. When the concentration of NaOH was too high, the flower-like ZnO formed was dissolved and destroyed by the excessively high concentration of NaOH, and the flower-like sodium titanate was not formed. In addition, it should be noted that too high a concentration of NaOH solution caused P25 nanoparticles to be peeled off so thinly that the edges of the sheets were curled and formed tubular or rod shape.

2.1.2. Spectral Properties

X-ray diffraction (XRD) patterns of P25 and Zn-Ti-6 synthesized through hydrothermal method were studied to probe the crystal structure in Figure 3a. All the diffraction peaks of P25 were in a good agreement with anatase and rutile TiO_2 (JCPDS No. 89-4921 and JCPDS No. 89-0552). It was observed that P25 was a mixed crystal structure of anatase and rutile, and the sharp diffraction peaks indicated good crystallinity. The diffraction peak positions of the prepared Zn-Ti-6 were not changed, but the diffraction peaks were significantly weakened or disappeared, indicating that its crystallinity was weakened [36]. In addition, the characteristic diffraction peaks of ZnO were not found in the XRD pattern of Zn-Ti-6, which suggested that the ZnO template had been removed [37].

Fourier transform infrared (FTIR) spectra of P25 and Zn-Ti-6 were shown in Figure 3b. Two absorption peaks were observed clearly in the FTIR of P25 and Zn-Ti-6. One was the broader absorption peak near 3300 cm^{-1} , which corresponded to adsorbed water. The other was a narrower absorption peak near 1630 cm^{-1} , which corresponded to the hydroxyl on the sample surface. However, the intensity of the absorption peaks of Zn-Ti-6 at these two places was significantly stronger than that of P25. This indicates that there were abundant hydroxyl groups on the surface of Zn-Ti-6 [38,39]. These abundant hydroxyl groups not only adsorbed pollutants but also trapped holes to generate Ti-OH^+ radicals, which benefited the adsorption and photocatalytic performance of Zn-Ti-6 [40]. In order to further characterize the structural evolution from P25 to Zn-Ti-6, Raman spectra were shown in Figure 3c. The Raman spectrum of P25 exhibited strong bands at 142, 396, 443, 516, and 636 cm^{-1} . In these Raman bands, 142, 396, 516, and 636 cm^{-1} all corresponded to the

vibration modes of the anatase phase. Among them, 516 cm^{-1} corresponded to the B_{1g}/A_{1g} vibration mode of the anatase phase, and the others corresponded to the E_g vibration mode of the anatase phase. The E_g vibration mode of rutile was 443 cm^{-1} . In the Raman spectrum of Zn-Ti-6, the Raman bands at 184, 272, 450, and 701 cm^{-1} were clearly shown, which corresponded to the vibration mode of monoclinic TiO_2 -based composite [41]. Among them, the Raman shift at 272 cm^{-1} was related to the breaking of symmetry caused by the bending of the TiO_6 layered structure during the lamellar formation; the Raman shift at 450 cm^{-1} represented the 2D lepidocrocite-type TiO_6 octahedron with the existence of the layer; the Raman shift at 701 cm^{-1} was due to the bending of TiO_6 [42]. In short, the two Raman spectrum lines were significantly different, reflecting the structure transition of the sample from P25 to Zn-Ti-6. In addition, the characteristic Raman bands of ZnO were not found in the Raman spectrum, indicating that ZnO had been removed [43].

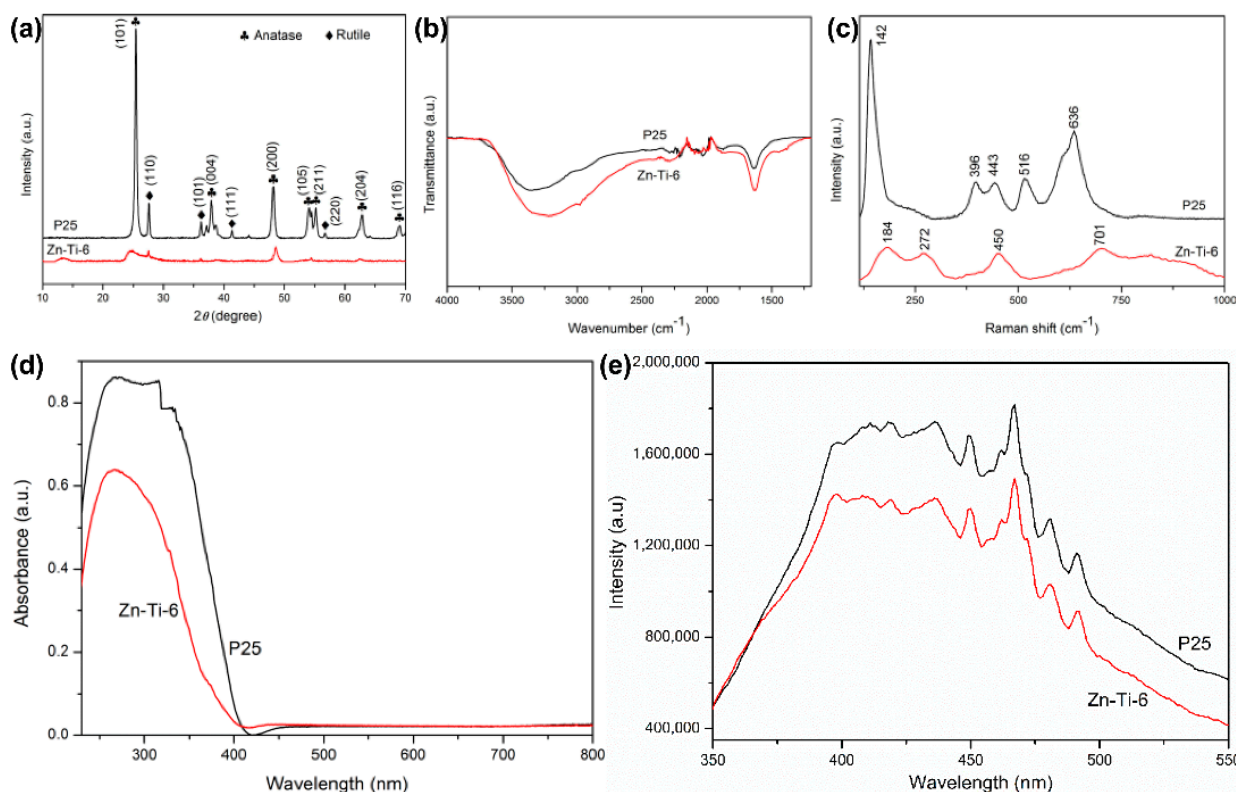


Figure 3. Optical properties: (a) XRD, (b) FTIR, (c) Raman, (d) UV-Vis diffuse reflectance spectra, and (e) photoluminescence spectra of P25 and Zn-Ti-6.

To investigate the light response ability of P25 and Zn-Ti-6, the UV-Vis diffuse reflectance spectra were depicted in Figure 3d. Clearly, P25 and Zn-Ti-6 both had strong ultraviolet light absorption characteristics near 400 nm, which was similar to the results of other studies [44–46]. As a non-destructive technique technology, photoluminescence spectroscopy was used to explore the separation efficiency of electron–hole pairs in semiconductor materials. Usually, lower fluorescence intensity represented a lower photogenerated carrier recombination rate [47]. Figure 3e showed the photoluminescence spectra of P25 and Zn-Ti-6 under the excitation wavelength at 300 nm. It can be observed that P25 and Zn-Ti-6 both exhibited photoluminescence peaks at 398, 411, 419, 436, 450, 467, 481, and 492 nm. The difference was that the intensities of all the fluorescence peaks of Zn-Ti-6 were significantly lower than that of P25, which implies that Zn-Ti-6 inhibited the recombination of photogenerated electron–hole pairs effectively, benefiting the photocatalytic performance of the material. Among these, the peaks at 450, 467, 481, and 492 nm were all defect peaks generated by fluorescence excitation of surface defects. The peaks at 450 and

467 nm were the defect peaks due to the excitation of band edge electrons, and the peaks at 481 and 492 nm were the defect peaks due to the fluorescence excitation of band-bound electrons [48,49].

2.2. Adsorption and Photocatalytic Activity Evaluation

The N₂ adsorption–desorption isotherms were shown in Figure 4. From the adsorption–desorption isotherms, it can be seen that the specific surface area from Brunauer–Emmett–Teller (BET) analysis of Zn-Ti-6 was 130.0 m²/g, which was much larger than P25 (48.0 m²/g). Additionally, the typical isotherms of P25 and Zn-Ti-6 were both type IV (Brunauer–Deming–Deming–Teller classification), with a hysteresis loop of type H3 at high relative pressure. This suggests the existence of slit-like mesopores in the samples. The difference was that the pores of P25 were formed by the disorderly accumulation of small particles, while the pores of Zn-Ti-6 were formed by the stacking of petals [50]. These were consistent with the results observed by FESEM and TEM. The high BET surface area and open mesoporous morphology were vital in increasing the number of sites for the adsorption and redox reaction [51]. These were beneficial to the adsorption and photocatalytic performance of Zn-Ti-6.

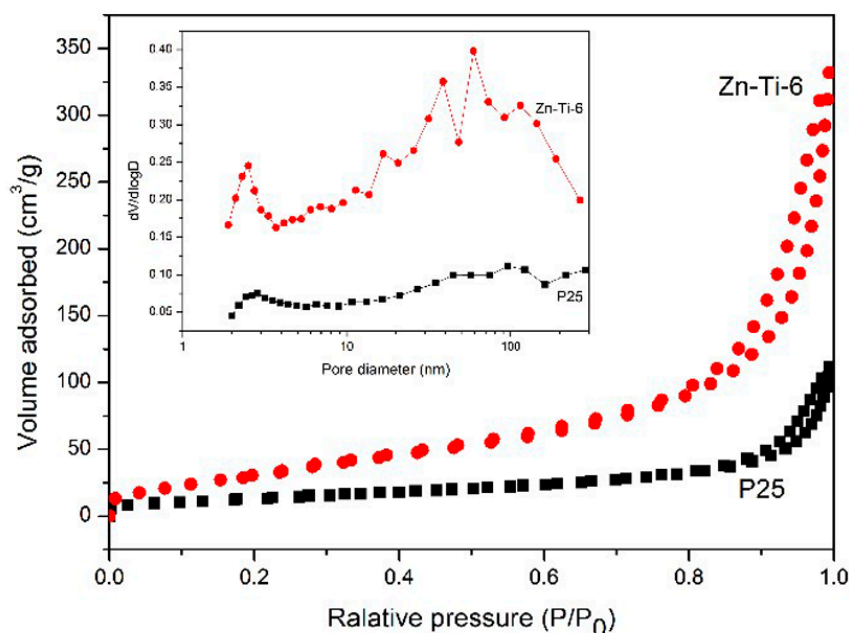


Figure 4. Typical N₂ adsorption–desorption isotherms and their corresponding pore size distribution curves (inset) of P25 and Zn-Ti-6.

In order to easily describe the process of sample adsorption and photocatalytic degradation of MB solution, the decontamination efficiency can be expressed as

$$\text{decontamination efficiency(\%)} = \left(1 - \frac{C_t}{C_0}\right) \times 100\% \quad (1)$$

where C_0 and C_t (mg/L) represent the initial concentration and the concentration at time t of the MB solution, respectively.

Adsorption and photocatalytic degradation of MB solution (60 mg/L, 50 mL) by P25 and Zn-Ti-6 were shown in Figure 5a, which was calculated and plotted according to Equation (1). The dark adsorption time ranged from −240 min to 0 min, and the photocatalytic degradation time ranged from 0 min to 240 min. It was clear that P25 had little adsorption capacity for MB, while Zn-Ti-6 had a strong adsorption capacity for MB solution. For Zn-Ti-6, the dark adsorption was very fast in the first 30 min, and decontamination efficiency reached 62.83%. This was because of the strong electrostatic

interaction between negatively charged Zn-Ti-6 and positively charged MB. Subsequently, the dark adsorption capacity slowed down. This could be explained by the fact that the adsorption vacancies on the surface of Zn-Ti-6 decreased, and the repulsion between MB molecules caused the adsorption rate to decrease with the extension of the adsorption time [48]. At 180 min, the dark adsorption reached equilibrium, and the decontamination efficiency was 73.30%, indicating that Zn-Ti-6 had a good adsorption capability. Under visible light irradiation, P25 showed weak photodegradation ability for MB, while Zn-Ti-6 exhibited better photodegradation ability for MB. In general, under dark adsorption and visible light irradiation, the decontamination efficiency of P25 for MB solution was only 2.70%, and the decontamination efficiency of Zn-Ti-6 for MB solution was 85.76%, which was about 32 times stronger than that of P25. This suggested that Zn-Ti-6 had a strong ability to remove the pollution of high-concentration MB solution through the adsorption–photocatalytic degradation method. The reasons for the above phenomena were as follows: there were a few adsorption sites on the surface of P25, and its specific surface area was small (BET was $48.0 \text{ m}^2/\text{g}$), which led to the poor adsorption capacity of P25 for MB. Notably, the adsorption capacity of P25 was too poor to be displayed when the pollutant was a high-chroma MB solution. In addition, although P25 had a good photocatalytic ability in the ultraviolet region, the photocatalytic ability in the visible region was very weak. A high chroma of the MB solution resulted in poor light transmission, which further led to the weak photodegradation ability of P25. In contrast, Zn-Ti-6 possessed the flower-like structure, the large specific surface area (BET was $130.0 \text{ m}^2/\text{g}$), and the rich surface hydroxyl groups, which helped to provide a large number of adsorption sites for MB, leading to the efficient adsorption ability of Zn-Ti-6. In addition, the flower-like structure, the surface abundant hydroxyl groups, and the strong adsorption capacity for MB were conducive to take full advantage of light, which was favorable for the photodegradation of MB by Zn-Ti-6.

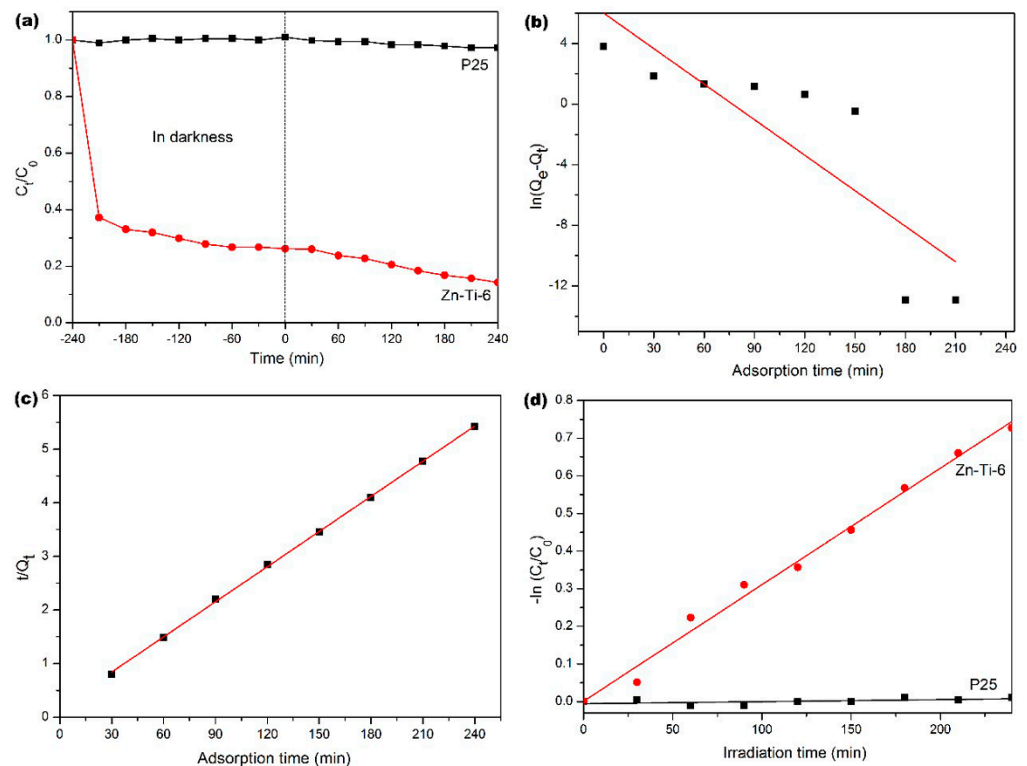


Figure 5. (a) Adsorption and photocatalytic degradation of MB solution (60 mg/L, 50 mL) by P25 and Zn-Ti-6. Adsorption kinetic models in the linear transformation for Zn-Ti-6: (b) pseudo-first-order and (c) pseudo-second-order. (d) First-order kinetic fitting for P25 and Zn-Ti-6 photocatalytic degradation of MB solution.

The characteristics in the adsorption process can be further studied by the adsorption kinetics models. There are two commonly used adsorption kinetic models, the pseudo-first-order model (Equation (2)) and the pseudo-second-order model (Equation (3)):

$$\ln(Q_e - Q_t) = \ln Q_e - k_1 t \quad (2)$$

$$\frac{t}{Q_t} = \left(\frac{1}{Q_e}\right)t + \frac{1}{k_2 Q_e^2} \quad (3)$$

where k_1 and k_2 (min^{-1}) represent the rate constants of the pseudo-first-order model and the pseudo-second-order model, respectively; Q_t and Q_e (mg/g) represent the adsorption capacity of MB at time t and at adsorption equilibrium, respectively. The calculation equations of Q_t and Q_e are defined below:

$$Q_t = \frac{(C_0 - C_t)V}{W} \quad (4)$$

$$Q_e = \frac{(C_0 - C_e)V}{W} \quad (5)$$

where C_0 and C_t (mg/L) are defined above; C_e represents the concentration of the MB solution at equilibrium; V is the initial volume of the MB solution (L); and W is the mass of the adsorbent used (g).

Figure 5b,c are the pseudo-first-order model and the pseudo-second-order model diagrams based on Equations (2) and (3) for the adsorption of MB onto Zn-Ti-6, respectively. It can be seen that the adsorption of MB onto Zn-Ti-6 conformed to the pseudo-second-order model (correlation coefficient $R^2 = 0.9999$, the rate constant $k_2 = 0.0218 \text{ min}^{-1}$). The equilibrium adsorption capacity calculated by the pseudo-second-order model was 45.8716 mg/g, which was in good agreement with the equilibrium adsorption capacity obtained by experiments of 43.9790 mg/g. This indicated that the adsorption process could be well described by the pseudo-second-order kinetics model.

The pseudo-first-order kinetics model is still used to describe the rate constant of dye photodegradation with respect to the degradation time, and the relationship is described in Equation (6):

$$\ln\left(\frac{C_t}{C_0}\right) = -kt \quad (6)$$

where C_0 and C_t are defined above, and k is the pseudo-first-order kinetics model rate constant (min^{-1}).

According to Equation (6), the first-order kinetics model of P25 and Zn-Ti-6 was as shown in Figure 5d for the stage of photodegradation of MB. The good linear correlation confirmed that both of the photodegradation processes followed the pseudo-first-order kinetics. In contrast, the rate constant k of P25 was very small, while the rate constant k of Zn-Ti-6 was larger, at 0.0031 min^{-1} . This showed that Zn-Ti-6 had a positive photodegradation effect on MB compared with P25.

3. Materials and Methods

All of the chemicals were analytical grade and used without any further purification. P25 was purchased from Degussa Co. Ltd., China. NaOH, HCl, $\text{Zn}(\text{NO}_3)_2 \cdot 6\text{H}_2\text{O}$, ethyl alcohol, and MB were purchased from Sinopharm Chemical Reagent Co. Ltd., Shanghai, China. Deionized water was used throughout the experiments.

In a typical synthesis procedure, 0.8 g of P25 was dispersed in 50 mL of different molar concentrations of NaOH solution. The solution was kept under magnetic stirring for 30 min. Subsequently, a certain amount of $\text{Zn}(\text{NO}_3)_2 \cdot 6\text{H}_2\text{O}$ solution was dropped slowly into the above suspensions. Then, the mixture was treated at 180°C for 6 h in a Teflon-lined autoclave of 100 mL. After the reaction was complete, the autoclave was cooled naturally to room temperature. The white precipitate was washed with deionized water until the

pH reached 7. Subsequently, the white precipitate was dispersed in 500 mL of diluted HCl solution overnight. Finally, the white precipitate was washed with deionized water and absolute ethanol, in order, and then dried at 60 °C for 12 h.

The morphological features of the samples were examined by FESEM (FEI Quanta-450, operated at 20 kV in high vacuum) (FEI, Hillsboro, OR, USA) and TEM (JEOL JEM-3010, operated at 100 kV)(JEOL, Tokyo, Japan). The crystalline phase data of the samples were collected by XRD (Rikagu MiniFlex600, Rikagu, Tokyo, Japan) with Cu K α radiation (wavelength = 1.54 Å). The diffractograms of samples were recorded in 2 θ from 10° to 70° at a step of 0.02°. The specific surface area and pore size distribution were measured by N₂ adsorption–desorption isotherm using the equipment (GW-BK100B, Beijing, China). FTIR spectra were determined by PerkinElmer Spotlight 400 & Frontier spectrometer (PerkinElmer, Waltham, MA, USA) to detect bonding structures and functional groups. Raman spectra were collected by Renishaw inVia Reflex Raman spectrometer (Renishaw, England) with an excitation wavelength of 514 nm. UV–Vis diffuse reflectance spectra of the samples were recorded on PerkinElmer Lambda 950 spectrometer (PerkinElmer, Waltham, MA, USA), and BaSO₄ was used as reflectance standard. The fluorescence spectra were analyzed by HORIBA FluoroMax+ fluorescence spectrometer (HORIBA, Irvine, CA, USA) with a Xe lamp as an excitation source to investigate the recombination efficiency of photogenerated electron–hole pairs.

The adsorption and photocatalytic activities of samples were evaluated by the degradation of MB solution. The instrument is a photochemical reaction system (Zhong Jiao Jin Yuan, Beijing, China). The light source was a 300 W Xe lamp, and a cut-off filter (420 nm) was used to simulate visible light. The Xe lamp was surrounded by water to keep a constant temperature. In the adsorption and photocatalytic reaction, the suspensions used were obtained by adding 0.05 g of samples into 50 mL of 60 mg/L MB solution, and the suspensions were under constant magnetic stirring. In order to investigate the regular pattern of adsorption with time, the suspensions were in the dark, and some MB solutions were removed at different time points. The Xe lamp was turned on to conduct the photocatalytic experiments after the adsorption–desorption equilibrium was established. Like dark adsorption, some MB solutions were removed at different photocatalytic reaction time points to explore the variation of photodegradation over time. Specifically, 1.6 mL of solutions were collected at the specified time points and centrifuged to separate the samples at a speed of 1500 r/min for 5 min. Following this, 0.8 mL of supernatant was removed and mixed with 2.4 mL of deionized water as the final test solutions. The concentrations of MB solution were gauged by iDH2000-BSC optical fiber spectrometer (ideaoptics, Shanghai, China).

4. Conclusions

In summary, TiO₂-based composite with flower-like morphology (denoted as Zn-Ti-6) was successfully fabricated by a facile alkaline hydrothermal procedure. NaOH was a morphology-directing agent and reactive etchant. The flower-like ZnO was synthesized and used as a sacrificial template. A possible formation mechanism was proposed. Zn-Ti-6 exhibited better adsorption and photocatalytic degradation capacity toward MB solution than P25, which was attributed to Zn-Ti-6 having a larger specific surface area, more abundant hydroxyls, and lower photoluminescence intensity than P25. For high-chroma wastewater, excellent adsorption performance is largely beneficial to the subsequent photocatalytic degradation performance. The adsorption data of Zn-Ti-6 fitted well with the pseudo-second-order kinetics model, and the photocatalytic degradation fitted with the pseudo-first-order kinetics model. Relying on the adsorption–photocatalytic degradation, MB was almost completely removed under visible light. Zn-Ti-6 synthesized by the alkaline hydrothermal process has the potential to combine with other photocatalytic material to further expand its application in adsorption–photocatalytic degradation of high-chroma wastewater.

Author Contributions: Conceptualization, M.T. and R.S.; methodology, M.T. and J.W.; validation, R.S.; data curation, M.Y.; writing—original draft preparation, M.T. and J.W.; visualization, L.L.; project administration, R.S., M.Y. and L.L.; project administration and supervision, R.S. All authors have read and agreed to the published version of the manuscript.

Funding: This research was funded by Key Research and Development Program of Shaanxi Province, grant number 2020KW-011; Science and Technology Plan Project of Xi'an, grant number 2020KJRC0026.

Data Availability Statement: Data is contained within the article.

Conflicts of Interest: The authors declare no conflict of interest.

References

1. Huang, Y.; Fan, W.; Long, B.; Li, H.; Zhao, F.; Liu, Z.; Tong, Y.; Ji, H. Visible light $\text{Bi}_2\text{S}_3/\text{Bi}_2\text{O}_3/\text{Bi}_2\text{O}_2\text{CO}_3$ photocatalyst for effective degradation of organic pollutants. *Appl. Catal. B Env.* **2016**, *185*, 68–76. [[CrossRef](#)]
2. Xing, B.; Dong, J.; Yang, G.; Jiang, N.; Liu, X.; Yuan, J. An insight into N, S-co doped activated carbon for the catalytic persulfate oxidation of organic pollutants in water: Effect of surface functionalization. *Appl. Catal. A Gen.* **2020**, *602*, 117714. [[CrossRef](#)]
3. Zhang, Y.F.; Yan, Y.J.; Bian, F.; Zhang, G. Adsorption of methylene blue in media industry pollution by GO-coated glass wool/EVA/EPDM foaming composite. *Appl. Mech. Mater.* **2014**, *448*, 115–118. [[CrossRef](#)]
4. Alvarenga, G.; Lima, J.P.; Goszczynski, A.C.; Rosa, C.H.; Rosa, G.R.; Lopes, T.J. Methylene blue adsorption by timbaúva (*Enterolobium contortisiliquum*)-derived materials. *Environ. Sci. Pollut. Res.* **2020**, *27*, 27893–27903. [[CrossRef](#)]
5. Zhao, K.; Zhao, G.; Li, P.; Gao, J.; Lv, B.; Li, D. A novel method for photodegradation of high-chroma dye wastewater via electrochemical pre-oxidation. *Chemosphere* **2010**, *80*, 410–415. [[CrossRef](#)]
6. Agustina, T.E.; Ang, H.M.; Vareek, V.K. A review of synergistic effect of photocatalysis and ozonation on wastewater treatment. *J. Photochem. Photobiol. C Photochem. Rev.* **2005**, *6*, 264–273. [[CrossRef](#)]
7. Fazal, T.; Razzaq, A.; Javed, F.; Hafeez, A.; Rashid, N.; Amjad, U.S.; Rehman, M.S.; Faisal, A.; Rehman, F. Integrating adsorption and photocatalysis: A cost effective strategy for textile wastewater treatment using hybrid biochar-TiO₂ composite. *J. Hazard. Mater.* **2020**, *390*, 121623. [[CrossRef](#)]
8. Gong, H.; Jin, Z.; Xu, H.; Wang, Q.; Zuo, J.; Wu, J.; Wang, K. Redesigning C and N mass flows for energy-neutral wastewater treatment by coagulation adsorption enhanced membrane (CAEM)-based pre-concentration process. *Chem. Eng. J.* **2018**, *342*, 304–309. [[CrossRef](#)]
9. Zhao, L.; Deng, J.; Sun, P.; Liu, J.; Ji, Y.; Nakada, N.; Qiao, Z.; Tanaka, H.; Yang, Y. Nanomaterials for treating emerging contaminants in water by adsorption and photocatalysis: Systematic review and bibliometric analysis. *Sci. Total Environ.* **2018**, *627*, 1253–1263. [[CrossRef](#)] [[PubMed](#)]
10. Banerjee, A.; Chattopadhyay, S.; Kundu, A.; Sharma, R.K.; Maiti, P.; Das, S. Vertically aligned zinc oxide nanosheet for high-performance photocatalysis of water pollutants. *Ceram. Int.* **2019**, *45*, 16821–16828. [[CrossRef](#)]
11. Lv, K.; Xu, Y. Effects of polyoxometalate and fluoride on adsorption and photocatalytic degradation of organic dye X3B on TiO₂: The difference in the production of reactive species. *J. Phys. Chem. B* **2006**, *110*, 6204–6212. [[CrossRef](#)] [[PubMed](#)]
12. Xu, C.; Wu, H.; Gu, F.L. Efficient adsorption and photocatalytic degradation of Rhodamine B under visible light irradiation over BiOBr/montmorillonite composites. *J. Hazard. Mater.* **2014**, *275*, 185–192. [[CrossRef](#)] [[PubMed](#)]
13. Lee, C.G.; Javed, H.; Zhang, D.; Kim, J.H.; Westerhoff, P.; Li, Q.; Alvarez, P.J. Porous electrospun fibers embedding TiO₂ for adsorption and photocatalytic degradation of water pollutants. *Environ. Sci. Technol.* **2018**, *52*, 4285–4293. [[CrossRef](#)] [[PubMed](#)]
14. Puma, G.L.; Bono, A.; Krishnaiah, D.; Collin, J.G. Preparation of titanium dioxide photocatalyst loaded onto activated carbon support using chemical vapor deposition: A review paper. *J. Hazard. Mater.* **2008**, *157*, 209–219. [[CrossRef](#)] [[PubMed](#)]
15. Khavina, E.Y. Nanoclays: Prospects from heterogeneous catalysts to a solid polymer film component. *Nanotechnol. Res. J.* **2016**, *9*, 123–144.
16. Yang, C.; Zhao, L.; Lu, X.; Pan, L.; Zhang, L.; Yan, W.; Zhao, Y.; Liu, Z. Preparation and photocatalysis of g-C₃N₄/zeolites based on photocatalytic activity and adsorption support ability. *Sci. Adv. Mater.* **2019**, *11*, 366–371. [[CrossRef](#)]
17. Augugliaro, V.; Yurdakal, S.; Loddo, V.; Palmisano, G.; Palmisano, L. Determination of photoadsorption capacity of polychrySTALLINE TiO₂ catalyst in irradiated slurry. *Adv. Chem. Eng.* **2009**, *36*, 1–35.
18. Li, Y.; Cao, S.; Zhang, A.; Zhang, C.; Qu, T.; Zhao, Y.; Chen, A. Carbon and nitrogen co-doped bowl-like Au/TiO₂ nanostructures with tunable size for enhanced visible-light-driven photocatalysis. *Appl. Surf. Sci.* **2018**, *445*, 350–358. [[CrossRef](#)]
19. Saha, S.; Wang, J.M.; Pal, A. Nano silver impregnation on commercial TiO₂ and a comparative photocatalytic account to degrade malachite green. *Sep. Purif. Technol.* **2012**, *89*, 147–159. [[CrossRef](#)]
20. Kasuga, T.; Hiramatsu, M.; Hoson, A.; Sekino, T.; Niihara, K. Formation of titanium oxide nanotube. *Langmuir* **1998**, *14*, 3160–3163. [[CrossRef](#)]
21. Tsai, C.C.; Teng, H. Structural features of nanotubes synthesized from NaOH treatment on TiO₂ with different post-treatments. *Chem. Mater.* **2006**, *18*, 367–373. [[CrossRef](#)]
22. López-Muñoz, M.J.; Revilla, A.; Alcalde, G. Brookite TiO₂-based materials: Synthesis and photocatalytic performance in oxidation of methyl orange and As (III) in aqueous suspensions. *Catal. Today* **2015**, *240*, 138–145. [[CrossRef](#)]

23. Naseri, K.; Allahverdi, A. Methylene blue adsorption by TiO₂-based nano-adsorbents: Performance evaluation and kinetic study. *Res. Chem. Intermed.* **2019**, *45*, 4863–4883. [[CrossRef](#)]
24. Cao, W.; Wang, W.; Shi, H.; Wang, J.; Cao, M.; Liang, Y.; Zhu, M. Hierarchical three-dimensional flower-like Co₃O₄ architectures with a mesocrystal structure as high capacity anode materials for long-lived lithium-ion batteries. *Nano Res.* **2018**, *11*, 1437–1446. [[CrossRef](#)]
25. Xie, S.; Zheng, B.; Kuang, Q.; Wang, X.; Xie, Z.; Zheng, L. Synthesis of layered protonated titanate hierarchical microspheres with extremely large surface area for selective adsorption of organic dyes. *CrystEngComm* **2012**, *14*, 7715–7720. [[CrossRef](#)]
26. Qi, Y.; Luan, Y.; Yang, M.; Wang, G.; Tan, L.; Li, J. Alkali concentration-dependent tailoring of highly controllable titanate nanostructures: From yolk-shell, hollow 3D nanospheres to 1D nanowires. *Appl. Surf. Sci.* **2014**, *293*, 359–365. [[CrossRef](#)]
27. Zhang, Y.; Li, G.; Liu, J.; Wang, T.; Wang, X.; Liu, B.; Liu, Y.; Huo, Q.; Chu, Z. Synthesis of hierarchical hollow sodium titanate microspheres and their application for selective removal of organic dyes. *J. Colloid Interface Sci.* **2018**, *528*, 109–115. [[CrossRef](#)] [[PubMed](#)]
28. Liu, M.; Piao, L.; Lu, W.; Ju, S.; Zhao, L.; Zhou, C.; Li, H.; Wang, W. Flower-like TiO₂ nanostructures with exposed {001} facets: Facile synthesis and enhanced photocatalysis. *Nanoscale* **2010**, *2*, 1115–1117. [[CrossRef](#)]
29. Paul, K.K.; Jana, S.; Giri, P.K. Tunable and high photoluminescence quantum yield from self-decorated TiO₂ quantum dots on fluorine doped mesoporous TiO₂ flowers by rapid thermal annealing. *Part. Part. Syst. Charact.* **2018**, *35*, 1800198. [[CrossRef](#)]
30. Hosono, E.; Matsuda, H.; Honma, I.; S Ichihara, M.; Zhou, H. Synthesis of a perpendicular TiO₂ nanosheet film with the superhydrophilic property without UV irradiation. *Langmuir* **2007**, *23*, 7447–7450. [[CrossRef](#)]
31. Zhao, X.; Lou, F.; Li, M.; Lou, X.; Li, Z.; Zhou, J. Sol–gel-based hydrothermal method for the synthesis of 3D flower-like ZnO microstructures composed of nanosheets for photocatalytic applications. *Ceram. Int.* **2014**, *40*, 5507–5514. [[CrossRef](#)]
32. Swain, P.S.; Rao, S.B.N.; Rajendran, D.; Pal, D.; Mondal, S.; Selvaraju, S. Effect of supplementation of nano zinc oxide on nutrient retention, organ and serum minerals profile, and hepatic metallothionein gene expression in wister albino rats. *Biol. Trace Elem. Res.* **2019**, *190*, 76–86. [[CrossRef](#)]
33. Hao, C.; Zhang, H.; Wang, X.; Shen, Y.; Yang, Y.; Zhao, Y. Hydrothermal synthesis of flower cluster-shaped ZnO microstructures with sodium lignosulfonate as structure-directing agent. *J. Mater. Sci. Mater. Electron.* **2015**, *26*, 9171–9177. [[CrossRef](#)]
34. De Souza, R.L.; Yu, H.; Rataboul, F.; Essayem, N. 5-Hydroxymethylfurfural (5-HMF) production from hexoses: Limits of heterogeneous catalysis in hydrothermal conditions and potential of concentrated aqueous organic acids as reactive solvent system. *Challenges* **2012**, *3*, 212–232. [[CrossRef](#)]
35. Chen, F.; Fang, P.; Liu, Z.; Gao, Y.; Liu, Y.; Dai, Y.; Luo, H.; Feng, J. Dimensionality-dependent photocatalytic activity of TiO₂-based nanostructures: Nanosheets with a superior catalytic property. *J. Mater. Sci.* **2013**, *48*, 5171–5179. [[CrossRef](#)]
36. Bavykin, D.V.; Kulak, A.N.; Walsh, F.C. Metastable nature of titanate nanotubes in an alkaline environment. *Cryst. Growth Des.* **2010**, *10*, 4421–4427. [[CrossRef](#)]
37. Caglar, Y.; Ilican, S.; Caglar, M. FESEM, XRD and DRS studies of electrochemically deposited boron doped ZnO films. *Mater. Sci. Pol.* **2017**, *35*, 824–829. [[CrossRef](#)]
38. Kim, T.W.; Lee, H.S.; Kim, D.H.; Jin, H.H.; Hwang, K.H.; Lee, J.K.; Park, H.C.; Yoon, S.Y. In situ synthesis of magnesium-substituted biphasic calcium phosphate and in vitro biodegradation. *Mater. Res. Bull.* **2012**, *47*, 2506–2512. [[CrossRef](#)]
39. Lin, L.; Zhang, X.; He, N.; Liu, J.; Xin, Q.; Guo, H. Operando dual beam FTIR study of hydroxyl groups and Zn Species over defective HZSM-5 zeolite supported zinc catalysts. *Catalysts* **2019**, *9*, 100. [[CrossRef](#)]
40. Asuha, S.; Zhou, X.G.; Zhao, S. Adsorption of methyl orange and Cr (VI) on mesoporous TiO₂ prepared by hydrothermal method. *J. Hazard. Mater.* **2010**, *181*, 204–210. [[CrossRef](#)]
41. Yoshida, K.; Miao, L.; Tanaka, N.; Tanemura, S. Direct observation of TiO₆ octahedron forming titanate nanotube by advanced transmission electron microscopy. *Nanotechnology* **2009**, *20*, 405709. [[CrossRef](#)]
42. Riss, A.; Elser, M.J.; Bernardi, J.; Diwald, O. Stability and photoelectronic properties of layered titanate nanostructures. *J. Am. Chem. Soc.* **2009**, *131*, 6198–6206. [[CrossRef](#)]
43. Lee, S.; Lee, S.H.; Paulson, B.; Lee, J.C.; Kim, J.K. Enhancement of local surface plasmon resonance (LSPR) effect by biocompatible metal clustering based on ZnO nanorods in Raman measurements. *Spectrochim. Acta Part A Mol. Biomol. Spectrosc.* **2018**, *204*, 203–208. [[CrossRef](#)]
44. Wang, A.N.; Teng, Y.; Hu, X.F.; Wu, L.H.; Huang, Y.J.; Luo, Y.M.; Christie, P. Diphenylarsinic acid contaminated soil remediation by titanium dioxide (P25) photocatalysis: Degradation pathway, optimization of operating parameters and effects of soil properties. *Sci. Total Environ.* **2016**, *541*, 348–355. [[CrossRef](#)] [[PubMed](#)]
45. Peng, Y.P.; Lo, S.L.; Ou, H.H.; Lai, S.W. Microwave-assisted hydrothermal synthesis of N-doped titanate nanotubes for visible-light-responsive photocatalysis. *J. Hazard. Mater.* **2010**, *183*, 754–758. [[CrossRef](#)] [[PubMed](#)]
46. Feng, M.; You, W.; Wu, Z.; Chen, Q.; Zhan, H. Mildly alkaline preparation and methylene blue adsorption capacity of hierarchical flower-like sodium titanate. *ACS Appl. Mater. Interfaces* **2013**, *5*, 12654–12662. [[CrossRef](#)] [[PubMed](#)]
47. Li, Q.; Anpo, M.; Wang, X. Application of photoluminescence spectroscopy to elucidate photocatalytic reactions at the molecular level. *Res. Chem. Intermed.* **2020**, *46*, 4325–4344. [[CrossRef](#)]
48. Zhang, W.F.; Zhang, M.S.; Yin, Z.; Chen, Q. Photoluminescence in anatase titanium dioxide nanocrystals. *Appl. Phys. B* **2000**, *70*, 261–265. [[CrossRef](#)]

49. Pushpavathi, N.; Sandhya, K.L.; Prasad, S.K. Effect of graphene flakes, Titanium dioxide and zinc oxide nanoparticles on the birefringence, I–V characteristics and Photoluminescence properties of liquid crystal. *J. Mol. Liq.* **2020**, *302*, 112571. [[CrossRef](#)]
50. Sing, K.S. Reporting physisorption data for gas/solid systems with special reference to the determination of surface area and porosity (Recommendations 1984). *Pure Appl. Chem.* **1985**, *57*, 603–619. [[CrossRef](#)]
51. Lapham, D.P.; Lapham, J.L. BET surface area measurement of commercial magnesium stearate by krypton adsorption in preference to nitrogen adsorption. *Int. J. Pharm.* **2019**, *568*, 118522. [[CrossRef](#)] [[PubMed](#)]